Supplementary Information for:

Isotopic analyses of Ordovician-Silurian siliceous skeletons indicate silica-depleted Paleozoic oceans

Contents

This supplementary information document includes 12 figures and 2 tables. Dataset S1 is provided in a separate .xlsx file.

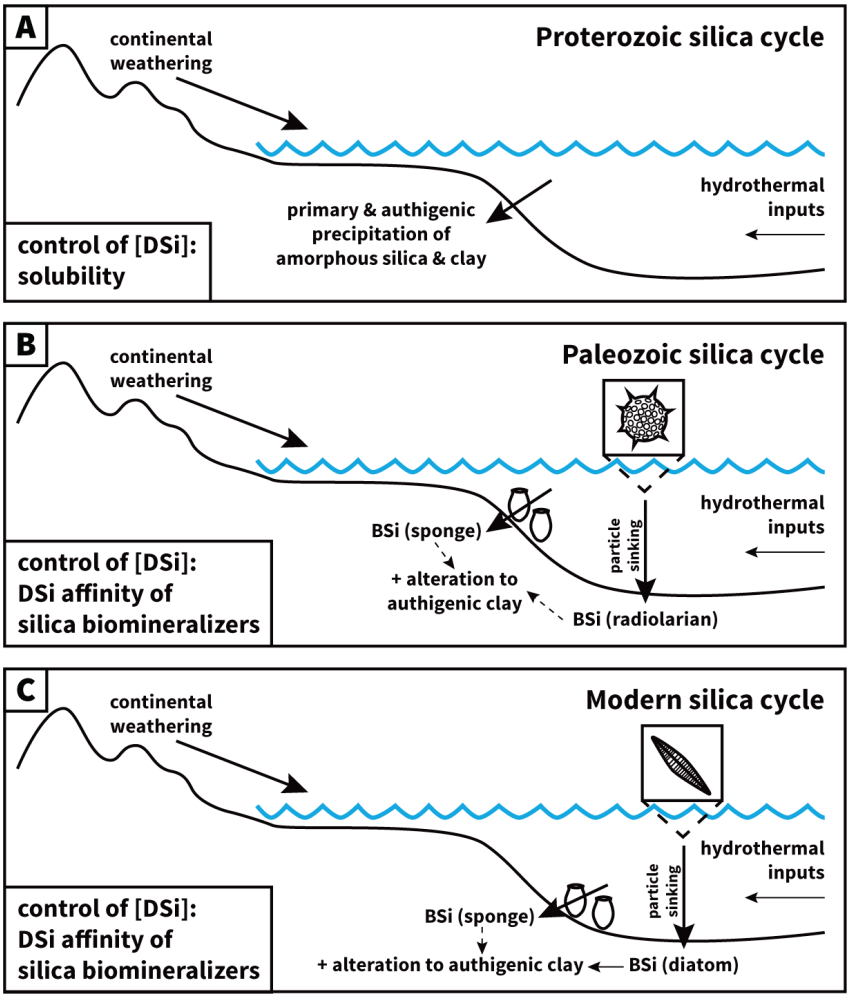

Figure S1—Simplified schematic illustrations of the Proterozoic (A), Paleozoic (B), and Modern (C) marine silica cycle. (A) In Proterozoic oceans, [DSi] is thought to have been controlled primarily by mineral solubilities—both amorphous silica and authigenic clay minerals—which were the major sinks for DSi delivered to seawater from continental weathering and hydrothermal inputs (Siever 1992). (B) In Paleozoic oceans, the marine silica cycle was impacted by the evolution of silica-biomineralizing organisms. BSi production in the water column (radiolarians) and on the seafloor (sponges) added new major sinks to balance DSi inputs. Early diagenetic alteration of these silica biominerals to authigenic clay minerals via reverse weathering reactions could have constituted an additional silica sink, but the reactivity of sponge spicules and radiolarian tests has not been well studied. (C) In modern oceans, BSi production in the water column (diatoms) and on the seafloor (sponges) constitute major silica sinks; precipitation of authigenic clay minerals via alteration of diatom frustules (i.e., reverse weathering) is an

additional important sink in the modern marine silica cycle (Rahman, Aller, and Cochran 2017; Tréguer and De La Rocha 2013).

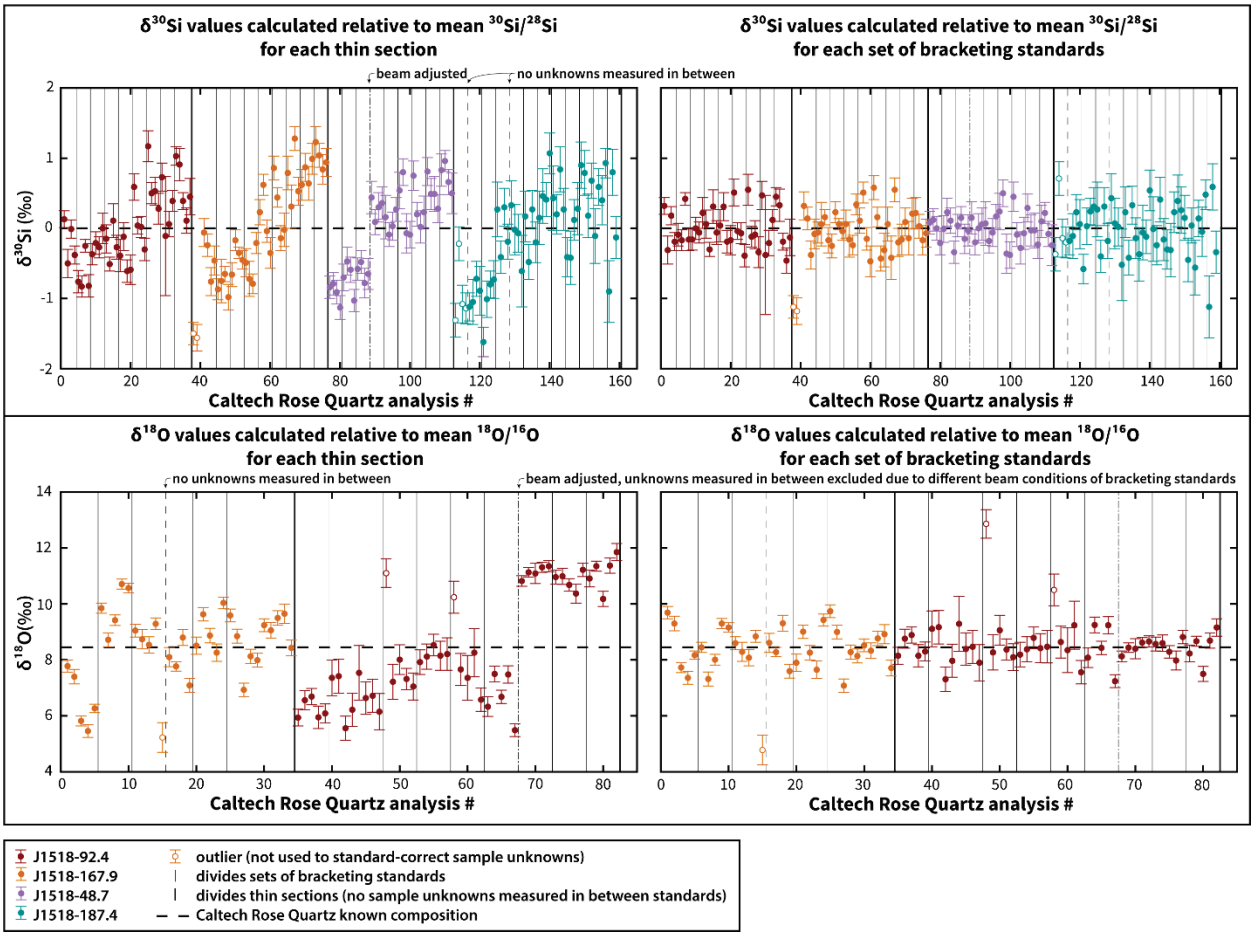

Figure S2—$\delta^{30}Si$ and $\delta^{18}O$ values of Caltech Rose Quartz reference material, calculated relative to mean isotope ratio across each thin section (left graphs) or relative to each set of bracketing standards (right graphs). Colors correspond to individual thin sections and vertical error bars indicate measurement precision of each individual analysis (1σ). Beam conditions were adjusted after sample changes (bold vertical lines) and at two points during analytical sessions of individual thin sections (dot-dash lines). Solid non-bold lines denote sets of bracketing standards; dashed non-bold lines indicate when no unknowns were measured between adjacent sets of bracketing standards. Open symbols note outliers not used to correct sample unknowns: n = 7 outliers were omitted from n = 160 total $\delta^{30}Si$ analyses of the Caltech Rose Quartz reference material and n = 3 outliers were omitted from n = 82 total $\delta^{18}O$ analyses of the Caltech Rose Quartz reference material. Sets of bracketing standards analyzed between every set of 7-14 sample unknowns allowed us to account for linear drift in instrumental mass fractionation during each analytical session (more pronounced for $\delta^{30}Si$ than $\delta^{18}O$).

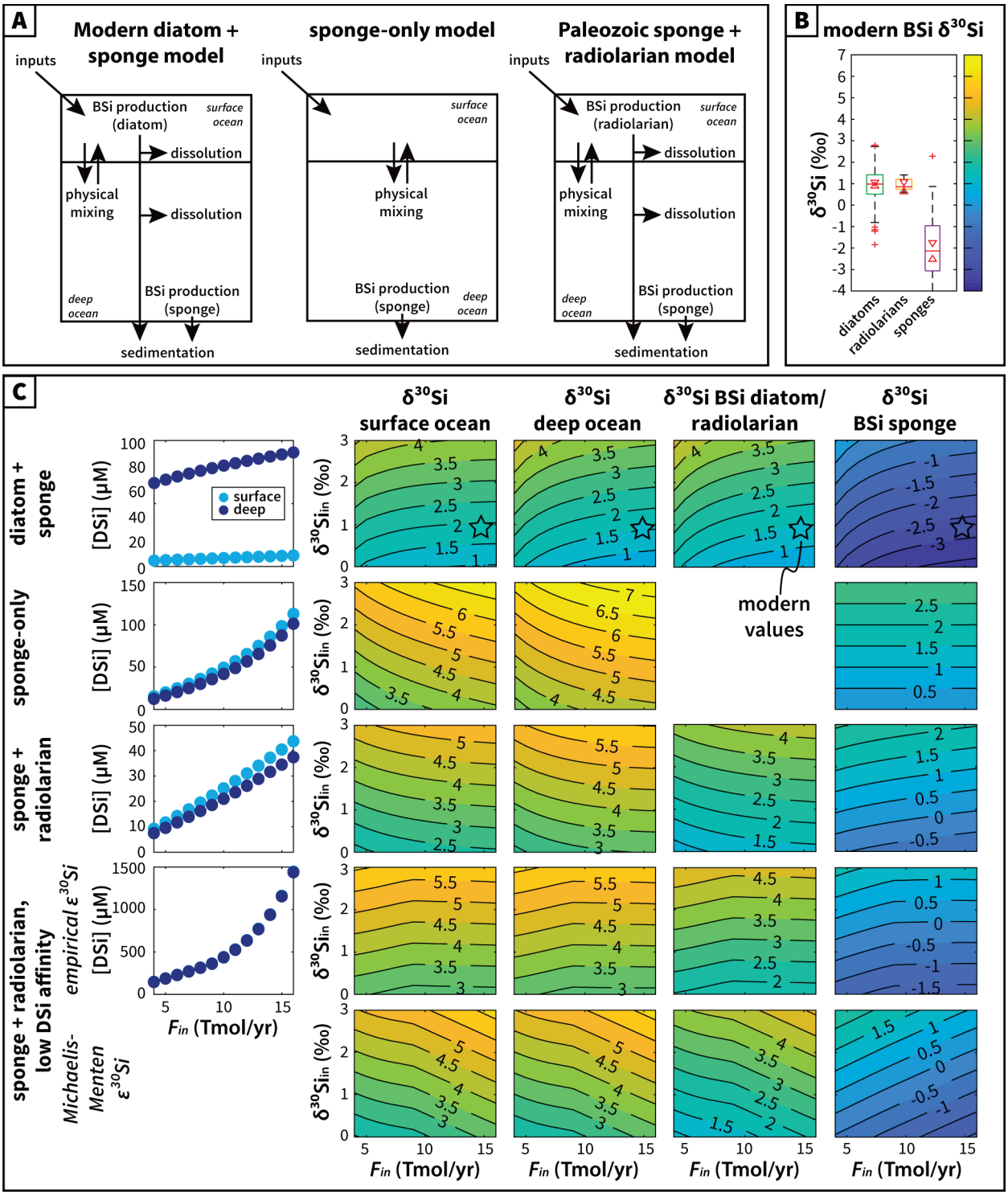

Figure S3—(A) Schematic illustrations of marine silica cycle models. (B) Box plots of $\delta^{30}Si$ distributions in modern marine BSi—diatoms (Cardinal et al. 2007; Fripiat et al. 2011; Hendry and Robinson 2012; De La Rocha, Brzezinski, and DeNiro 2000; Egan et al. 2012; Varela, Pride, and Brzezinski 2004), radiolarians (Abelmann et al. 2015), and sponge spicules (De La Rocha 2003; Hendry and Robinson 2012; Wille et al. 2010; Douthitt 1982) plotted next to the colorbar scale shown in (C). (C) Box model predictions: scatter plots of [DSi] for surface and deep oceans and contour plots $\delta^{30}Si$ values of surface

ocean, deep ocean, planktonic silica biomineralizers (diatoms or radiolarians), and sponges for five versions of the box model, from top to bottom: (1) diatom + sponge (with stars illustrating corresponding modern $\delta^{30}Si$ values colored following the same scale); (2) sponge-only; (3) sponge + radiolarian assuming modern DSi affinity and modern empirical $\varepsilon^{30}Si$-[DSi] calibration; (4) sponge + radiolarian assuming 20x lower DSi affinity than modern sponges and modern $\varepsilon^{30}Si$-[DSi] calibration; and (5) same as (4) but with Michaelis-Menten $\varepsilon^{30}Si$-[DSi] prediction. All plots share the same color scale shown in (B). [DSi] predictions are not shown for scenario (5) because they are identical to scenario (4).

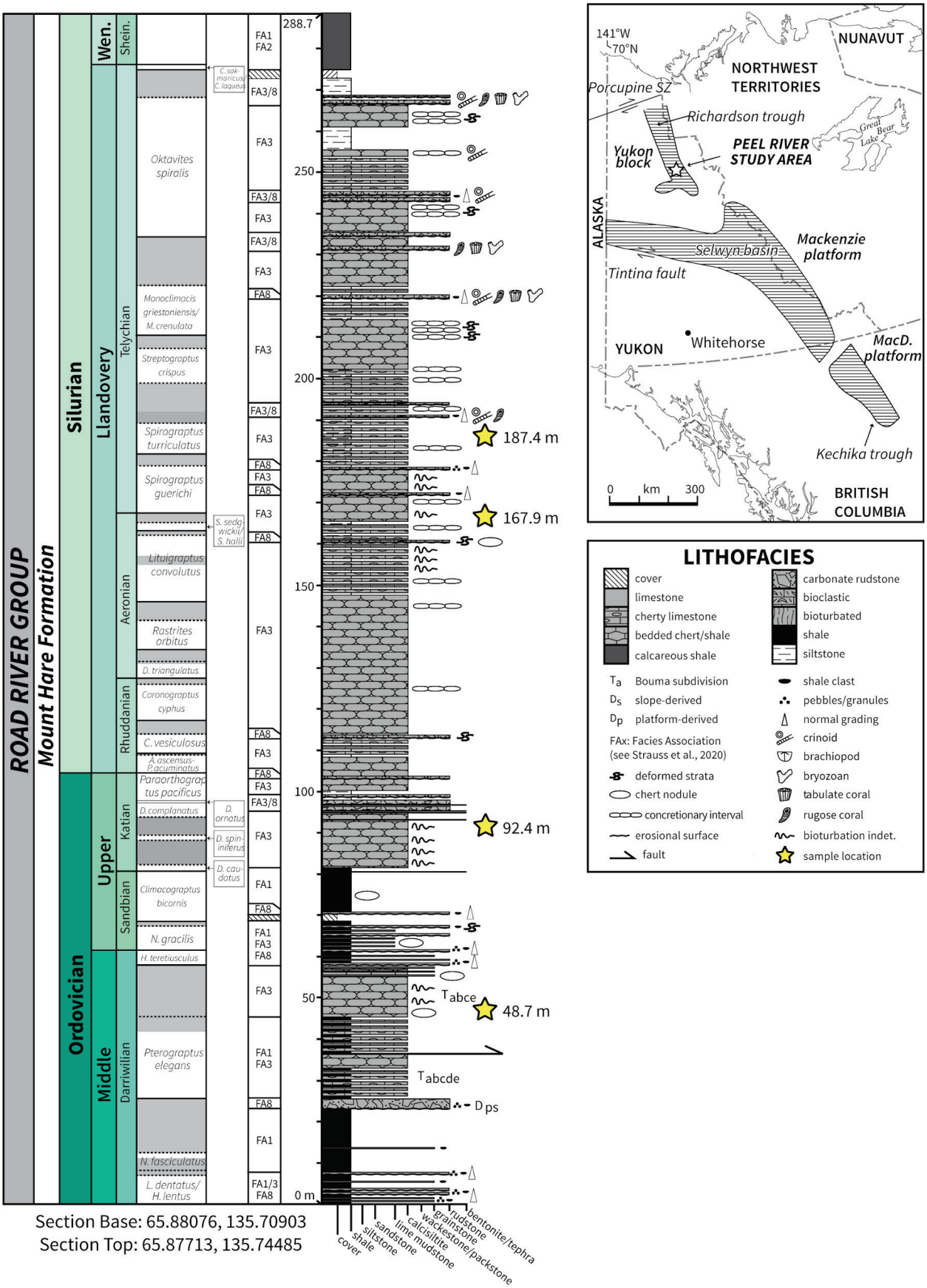
ROAD RIVER GROUP
Mount Hare Formation
Silurian
Ordovician
Wen.
Shein.
Llandovery
Upper
Middle
Telychian
Aeronian
Rhuddanian
Katian
Sandbian
Darriwilian
Oktavites spiralis
Monoclimacis griestoniensis/ M. crenulata
Streptograptus crispus
Spirograptus turriculatus
Spirograptus guerichi
Lituigraptus convolutus
Rastrites orbitus
D. triangulatus
Coronograptus cyphus
C. vesiculosus
A. ascensus-P. acuminatus
Paraorthograptus pacificus
D. complanatus
Climacograptus bicornis
N. gracilis
H. teretiusculus
Pterograptus elegans
N. fasciculatus
L. dentatus/ H. lentus
C. sakmaricus/ C. laqueus
S. sedgwickii/ S. halli
D. ornatus
D. spiniferus
D. caudatus
FA1
FA2
FA3/8
FA3
FA8
FA1/3
288.7
250
200
150
100
50
0 m
187.4 m
167.9 m
92.4 m
48.7 m
Tabce
Tabcde
Dps
Section Base: 65.88076, 135.70903
Section Top: 65.87713, 135.74485
cover
shale
siltstone
sandstone
lime mudstone
calcisiltite
wackestone/packstone
grainstone
rudstone
bentonite/tephra
141°W
70°N
NUNAVUT
NORTHWEST TERRITORIES
Porcupine SZ
Richardson trough
Great Bear Lake
Yukon block
PEEL RIVER STUDY AREA
ALASKA
Mackenzie platform
Selwyn basin
Tintina fault
YUKON
Whitehorse
MacD. platform
Kechika trough
0 km 300
BRITISH COLUMBIA
LITHOFACIES
cover
limestone
cherty limestone
bedded chert/shale
calcareous shale
carbonate rudstone
bioclastic
bioturbated
shale
siltstone
Ta Bouma subdivision
Ds slope-derived
Dp platform-derived
FAx: Facies Association (see Strauss et al., 2020)
deformed strata
chert nodule
concretionary interval
erosional surface
fault
shale clast
pebbles/granules
normal grading
crinoid
brachiopod
bryozoan
tabulate coral
rugose coral
bioturbation indet.
sample location

Figure S4—Location map of study area and stratigraphic column of section J1518 from Strauss et al. (2020) illustrating stratigraphic heights, sedimentary facies, and ages of samples in this study.

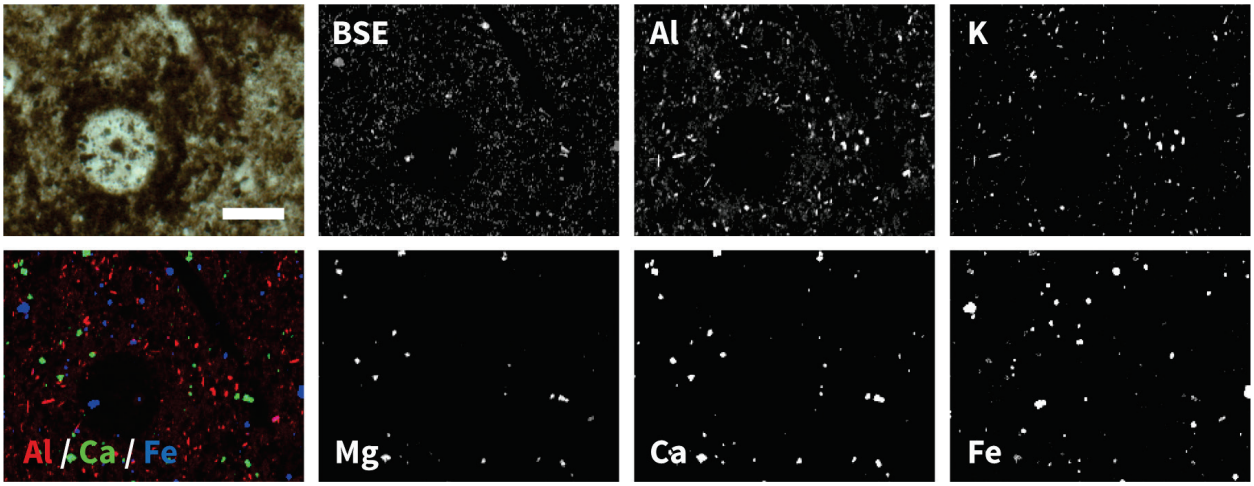

Figure S5—Additional electron microprobe elemental data of radiolarian and spicule from sample J1518-92.4, comparing transmitted light image (upper left); back-scattered electron (BSE) image; maps of elements Al, K, Mg, Ca, and Fe; and an RGB map plotting Al (red), Ca (green), and Fe (blue). Scale bar is 100 μm.

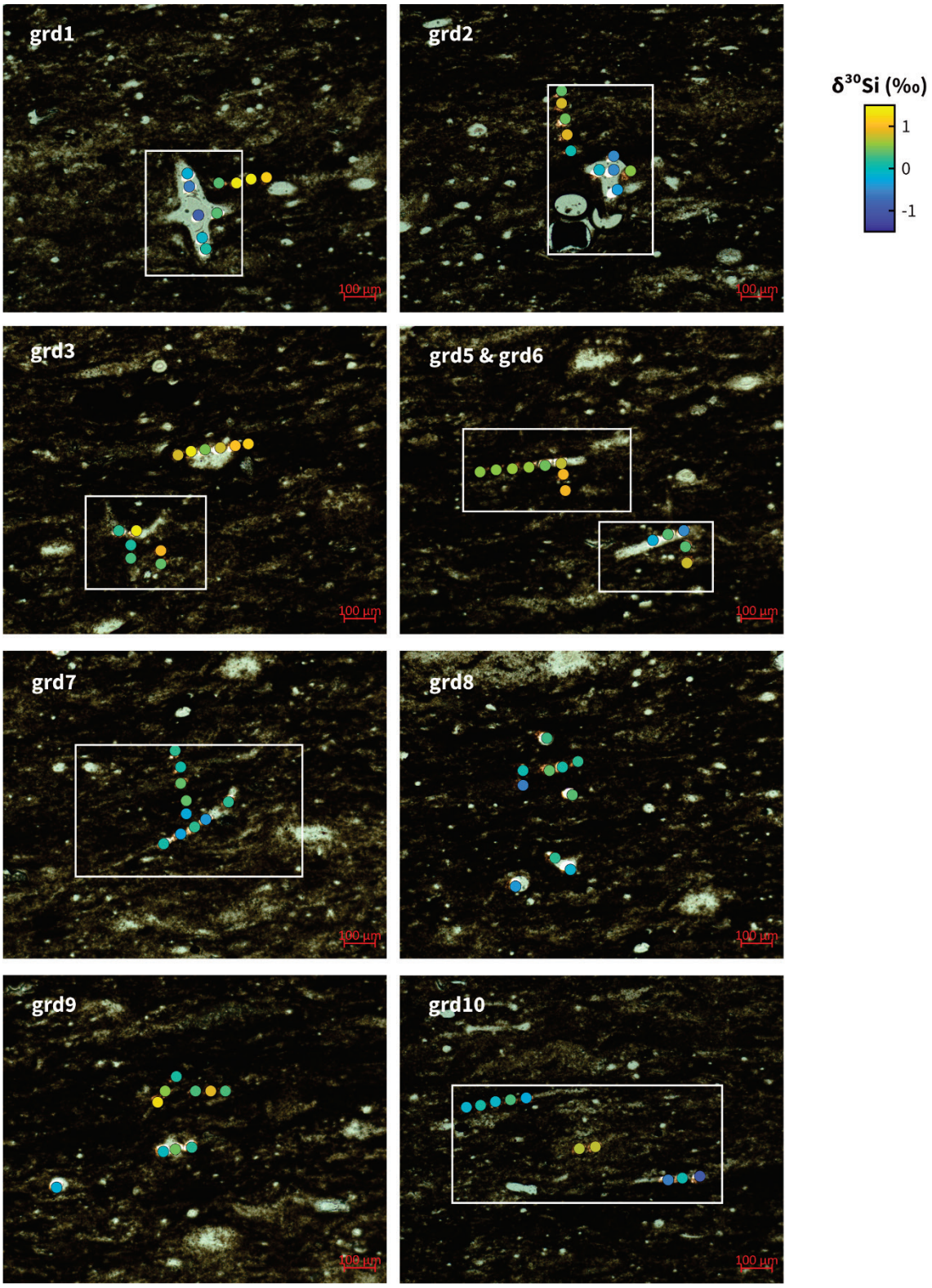

Figure S6—Plane-polarized transmitted light images of sample J1518 48.7 showing locations of $\delta^{30}Si$ analytical spots (circles, color-mapped by $\delta^{30}Si$ value). White boxes indicate approximate boundaries of EMP WDS maps collected from this sample. A higher resolution version of this image, a high resolution

map of the entire sample, and EMP WDS maps are archived in the linked OSF data repository at doi: 10.17605/OSF.IO/4AES6.

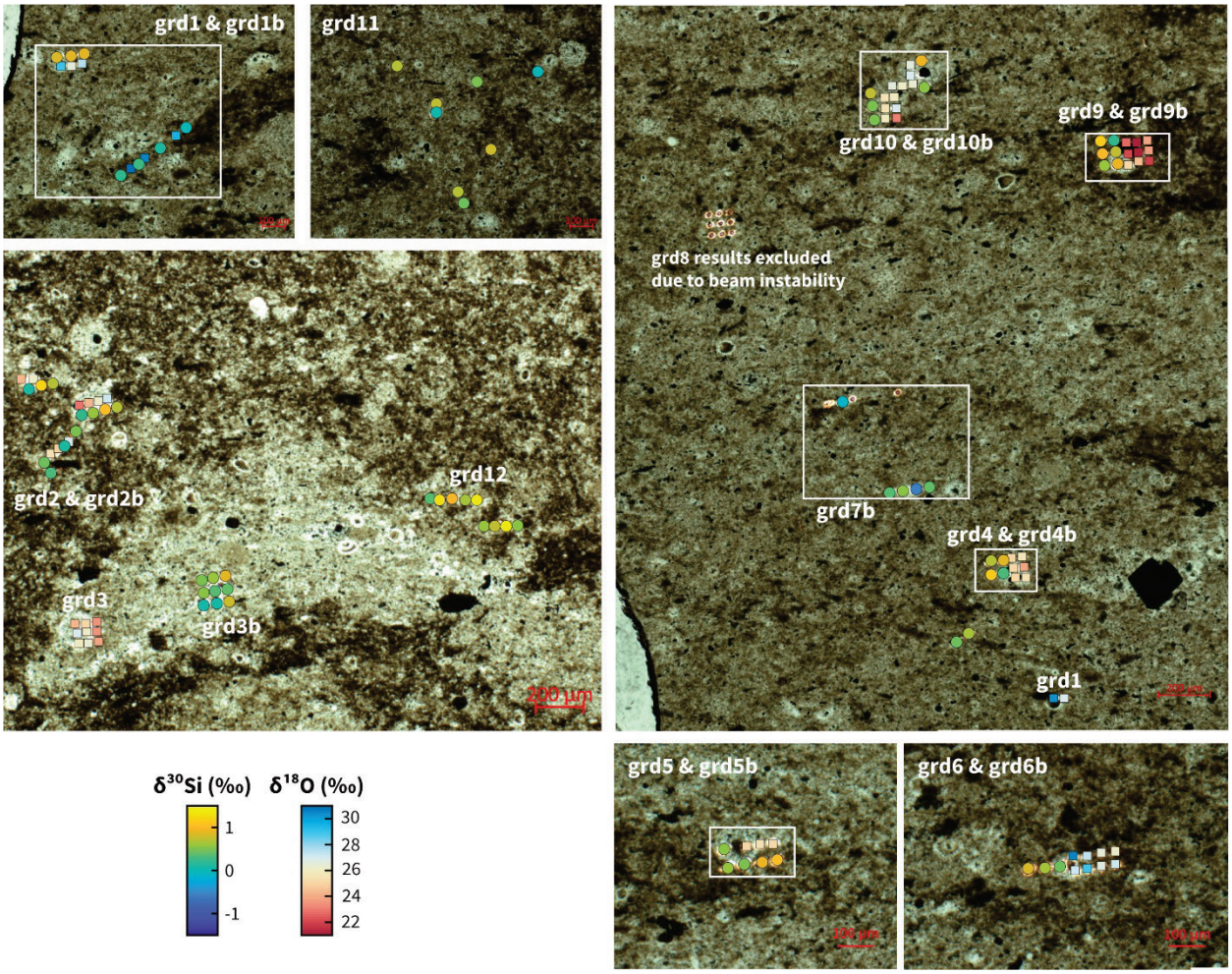

Figure S7— Plane-polarized transmitted light images of sample J1518 92.4 showing locations of $\delta^{30}Si$ and $\delta^{18}O$ analytical spots ($\delta^{30}Si$: circles, color-mapped by $\delta^{30}Si$ value; $\delta^{18}O$: squares, color-mapped by $\delta^{18}O$ value). White boxes indicate approximate boundaries of EMP WDS maps collected from this sample. A higher resolution version of this image, a high resolution map of the entire sample, and EMP WDS maps are archived in the linked OSF data repository at doi: 10.17605/OSF.IO/4AES6.

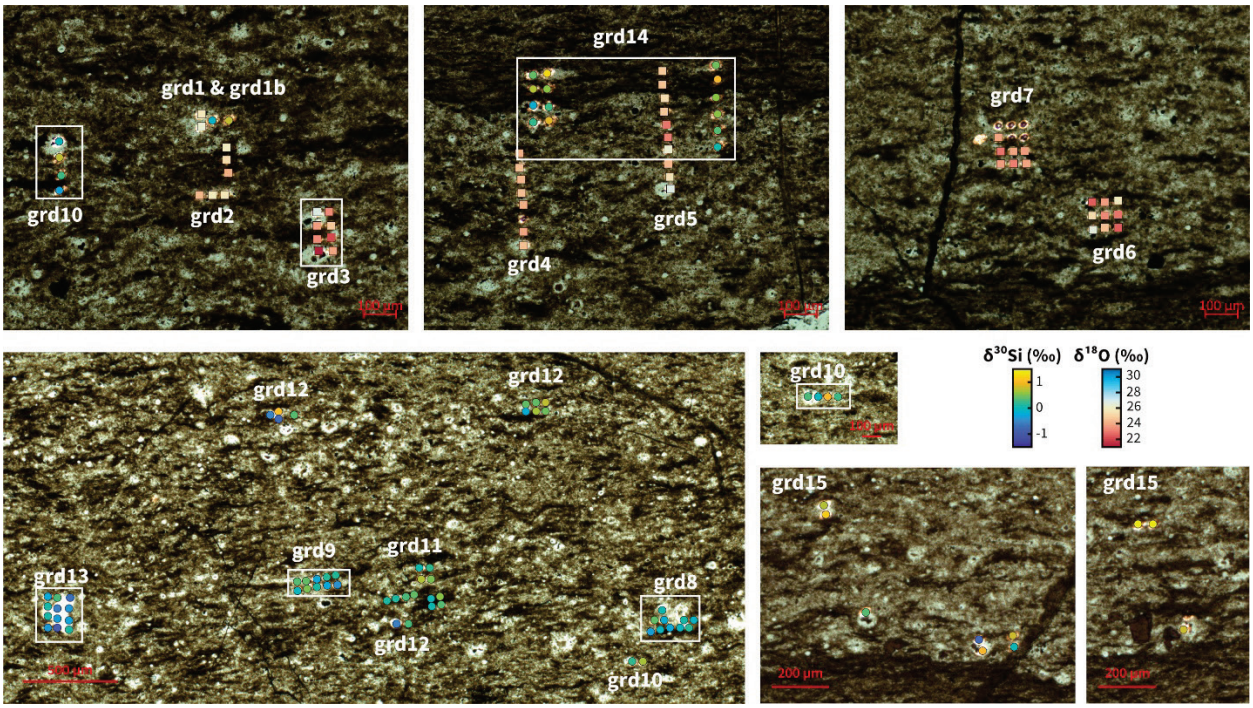

Figure S8— Plane-polarized transmitted light images of sample J1518 167.9 showing locations of $\delta^{30}Si$ and $\delta^{18}O$ analytical spots ($\delta^{30}Si$: circles, color-mapped by $\delta^{30}Si$ value; $\delta^{18}O$: squares, color-mapped by $\delta^{18}O$ value). White boxes indicate approximate boundaries of EMP WDS maps collected from this sample. A higher resolution version of this image, a high resolution map of the entire sample, and EMP WDS maps are archived in the linked OSF data repository at doi: 10.17605/OSF.IO/4AES6.

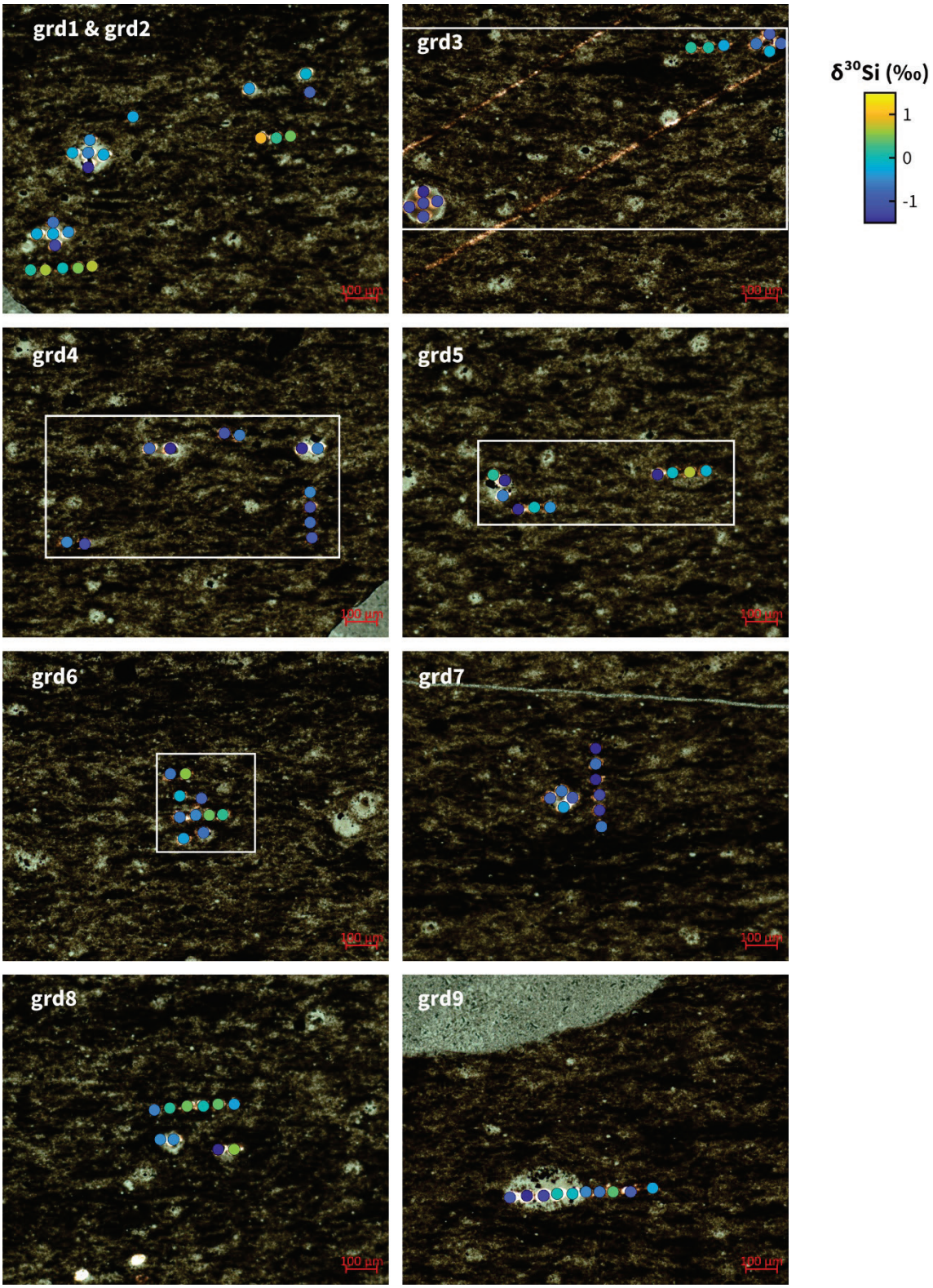

Figure S9— Plane-polarized transmitted light images of sample J1518 187.4 showing locations of $\delta^{30}Si$ (circles, color-mapped by $\delta^{30}Si$ value). White boxes indicate approximate boundaries of EMP WDS maps collected from this sample. A higher resolution version of this image, a high resolution map of the entire

sample, and EMP WDS maps are archived in the linked OSF data repository at doi: 10.17605/OSF.IO/4AES6.

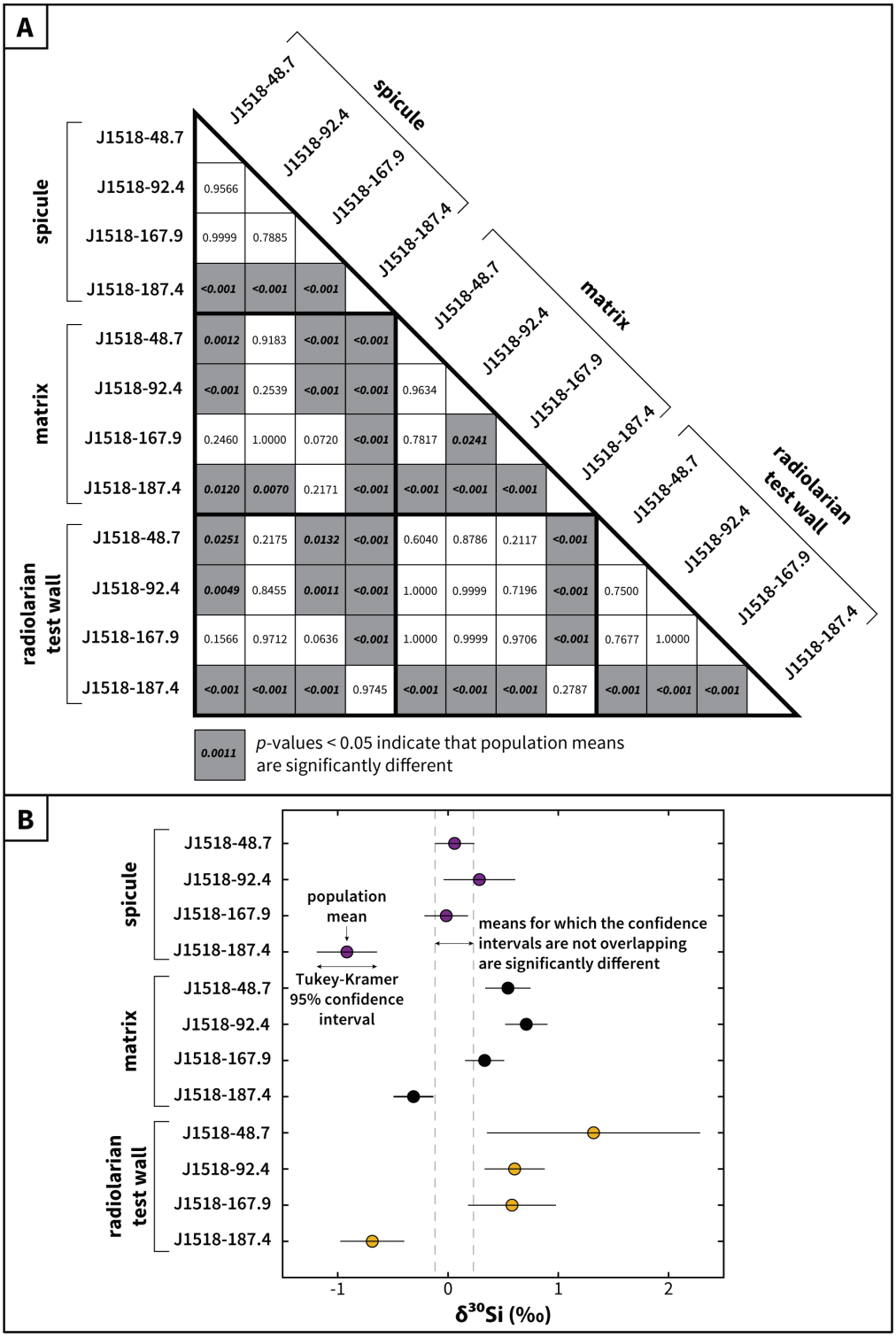

Figure S10— Results of post-hoc multiple comparison analysis (following the Tukey-Kramer procedure) based on an unbalanced 2-way ANOVA (ANalysis Of Variance) performed on SIMS $\delta^{30}Si$ data grouped

by sample ID and microfabric (spicule, matrix, radiolarian test wall; radiolarian interiors were excluded because no spots of this type were analyzed in sample J1518-167.9). (A) Matrix of *p*-values for every pair of sample-microfabric combination; grey cells with bold italic text indicate combinations for which the population means are significantly different. (B) Alternative visualization of the same information as in (A), where colored circles indicate population means and horizontal lines indicate 95% confidence intervals; means for which the confidence intervals do not overlap are significantly different (e.g., means for which the confidence intervals are outside the dashed grey lines are significantly different from spicules in sample J1518-48.7). This analysis indicated that the populations of spicules within samples J1518-48.7, J1518-92.4, and J1518-167.9 were not significantly different from each other and that the populations of radiolarian test walls within samples J1518-48.7, J1518-92.4, and J1518-167.9 were not significantly different from each other. For this ANOVA, the F-values were 70.59, 28.37, and 2.34 (corresponding *p*-values 4.9×10^{-35}, 4.6×10^{-12}, and 0.0315) for groupings of sample ID, microfabric, and sample ID * microfabric, respectively—indicating that differences between means grouped by sample, microfabric, and microfabric within sample are significant.

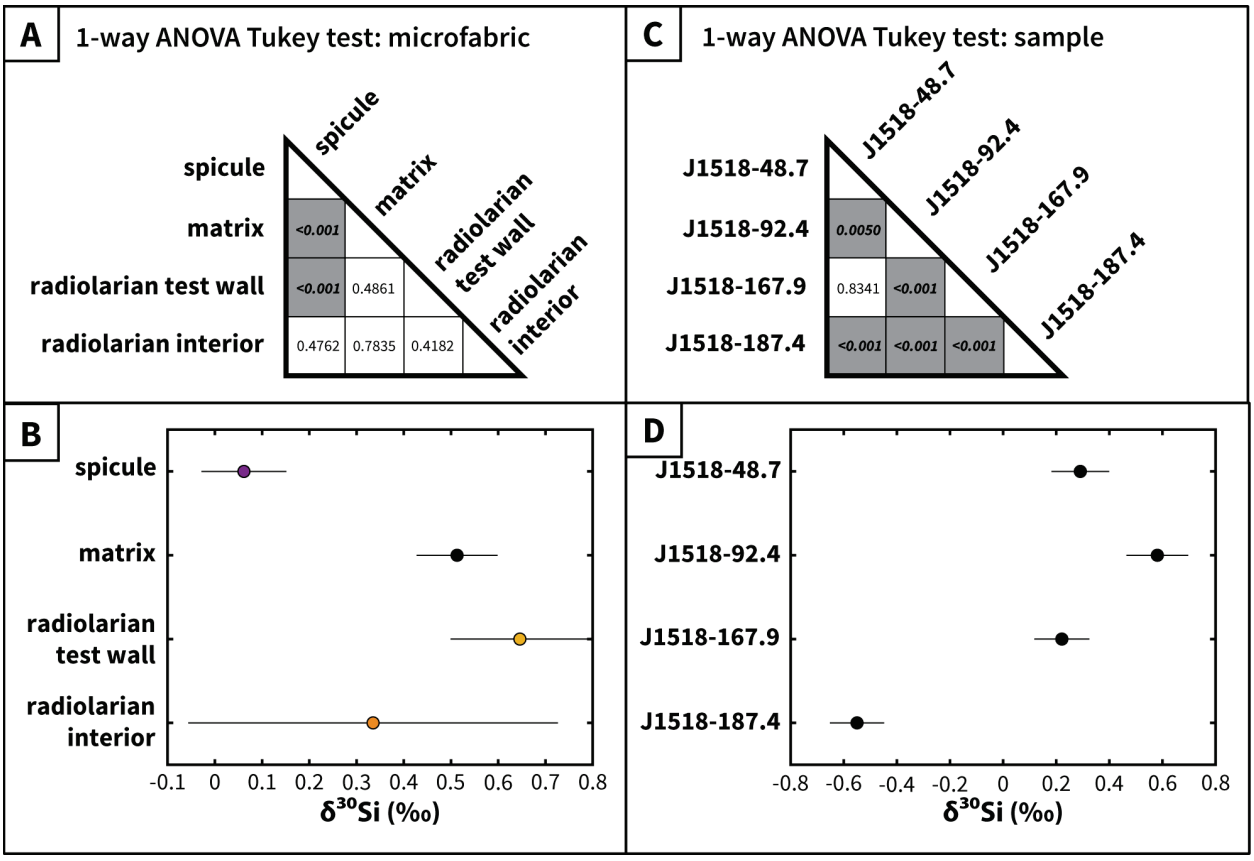

Figure S11— Results of post-hoc multiple comparison analysis (following the Tukey-Kramer procedure) based on an unbalanced 1-way ANOVA on SIMS δ^{30}Si data grouped by microfabric (A, B) and sample (C, D), following the same figure design as in Figure S10 and described in the Figure S10 caption. (A, B) Here, data were grouped only by microfabric, so analyses of the same microfabric are combined across all samples. Sample J1518-187.4 was excluded from this analysis because the Tukey test of the unbalanced 2-way ANOVA (Figure S10) demonstrated that the means of all microfabrics in this sample were significantly different from the means of all microfabrics in the remaining samples (except for the pair J1518-187.4 matrix – J1518-167.9 spicule), supporting the interpretation that this sample may have been more strongly affected by diagenesis. This analysis indicated that the population means of spicules and radiolarian test walls among these three samples are significantly different. For this ANOVA, the F-value was 22.46 and the *p*-value was 6.7×10^{-13}, indicating that differences between means grouped by microfabric were significant. (C, D) Here, data were grouped only by sample, so analyses of all microfabrics in each sample were combined. This analysis indicated that the population means (of all microfabric types) were significantly different among all pairs of samples except for the pair J1518-48.7 – J1518-167.9. We attributed some of these differences to the different numbers of analyses of each fabric type within each sample (i.e., different mixtures of the apparent end-member fabric compositions illustrated in panel B) and apparent diagenetic influence on sample J1518-187.4. For this ANOVA, the F-value was 68.43 and the *p*-value was 9.999×10^{-39}, indicating that differences between means grouped by sample were significant.

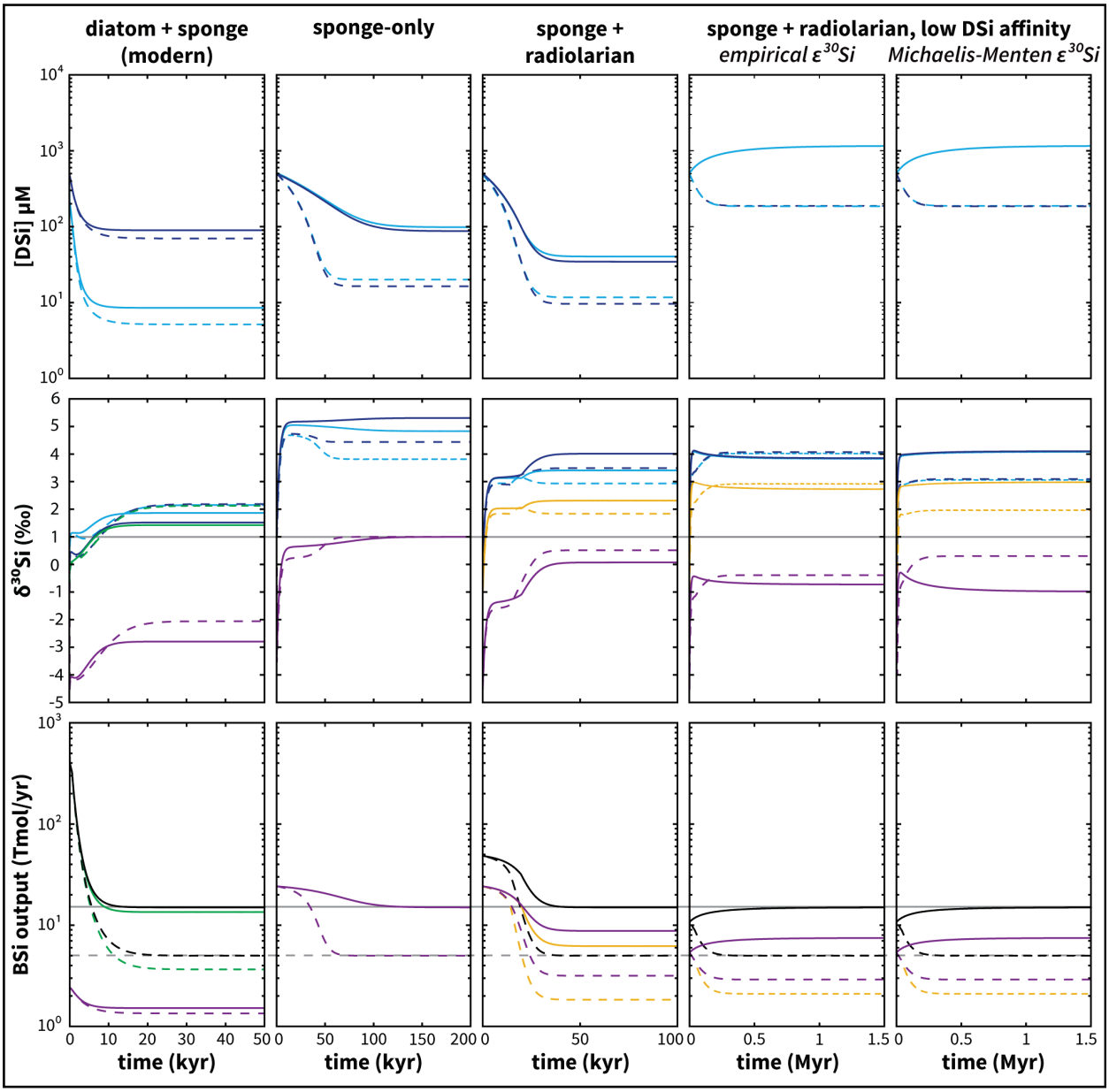
diatom + sponge (modern)
sponge-only
sponge + radiolarian
sponge + radiolarian, low DSi affinity
empirical ε30Si
Michaelis-Menten ε30Si
[DSi] µM
δ30Si (‰)
BSi output (Tmol/yr)
time (kyr)
time (Myr)

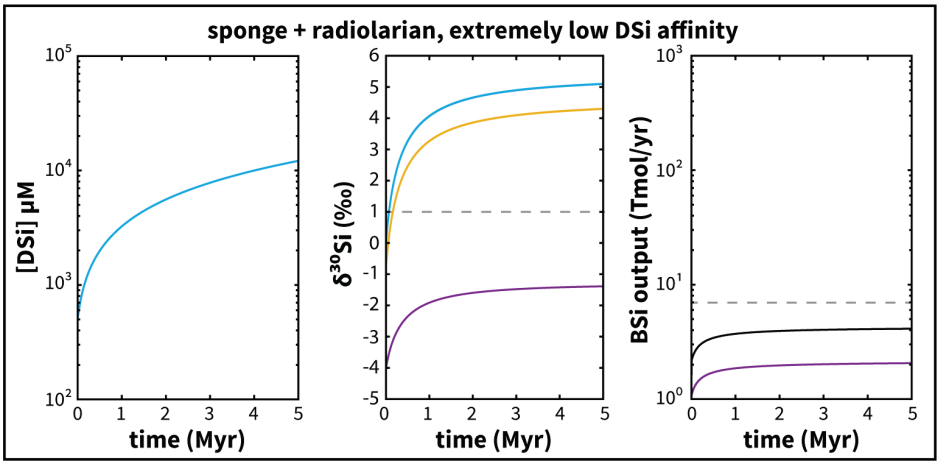
sponge + radiolarian, extremely low DSi affinity
[DSi] µM
δ30Si (‰)
BSi output (Tmol/yr)
time (Myr)
Fin (Tmol/yr)
15
5
surface ocean
deep ocean
diatom
radiolarian
sponge
BSi output sum
input

Figure S12—Evolution of [DSi], $\delta^{30}Si$, and BSi output flux over time for different box model versions, illustrating approach to steady state. The plots in the upper panel correspond to the models shown in Figure S3A for F_{in} = 5 Tmol/yr (dashed lines) or 15 Tmol/yr (solid lines) and $\delta^{30}Si_{in}$ = 1‰. The plots in the lower panel illustrate similar model parameters to those in the low DSi affinity with Michaelis-Menten $\varepsilon^{30}Si$ from the upper panel, but with DSi affinity reduced further. Under these conditions, [DSi] can exceed 1000 µM, but the model fails to reach steady state after 5 Ma (a significantly longer duration than in the models in the upper panel) because BSi production cannot keep pace with F_{in} and [DSi] continues to rise beyond abiotic mineral saturation thresholds (abiotic precipitation is not included in this model). The plots in the upper panel also illustrate that $\delta^{30}Si_{sponge}$ only transiently records extremely low values ~-4‰ and that under Paleozoic conditions, we expect $\delta^{30}Si_{sponge}$ > -2‰ and that both surface and deep ocean $\delta^{30}Si_{DSi}$ were ≥ 3‰.

Table S1—Parameters for box models

Parameter	**Diatom + sponge model**	**Sponge-only model**	**Sponge + radiolarian modern DSi affinity model**	**Sponge + radiolarian low DSi affinity model**
Ocean volume (m^3)	1.37×10^{18}			
Ocean surface area (m^2)	3.6×10^{4}			
Fraction of euphotic zone (dimensionless)	0.0263			
Physical mixing flux (m^3/yr)	1.37×10^{18} (De La Rocha and Bickle 2005)			
Particle sinking velocity, surface ocean (m/yr)	1800 (Passow, French, and Robert 2011)			
Particle sinking velocity, deep ocean (m/yr)	73000 (Passow, French, and Robert 2011)			
Maximum BSi production rate, V_{max}	Diatoms: 5×10^{14} mol/yr (Sarmiento and Gruber 2006); sponges: 0.13 µmol/hr/mL sponge volume (Maldonado et al. 2011)	0.13 µmol/hr/mL sponge volume (Maldonado et al. 2011)	0.13 µmol/hr/mL sponge volume (Maldonado et al. 2011); radiolarians assumed to have same V_{max} when scaled to mol/yr	0.05 µmol/hr/mL sponge volume; ~2.5x lower than the lowest value observed in modern sponges (López-Acosta et al. 2018)

Sponge seafloor density	0.34 L sponge / m^2; sponge-poor oligotrophic Mediterranean estimate (Maldonado et al. 2011)			
Fraction of seafloor colonized by sponges	0.025	0.2		
K_m (µM)	Diatom: 9 (Nelson et al. 1995; Amo and Brzezinski 1999); sponge: 75 (Maldonado et al. 2011)	75 (Maldonado et al. 2011)	75 (Maldonado et al. 2011); radiolarians assumed to have the same K_m	500; ~5x higher than the highest value observed in modern sponges (López-Acosta et al. 2018)
BSi dissolution rate constant, surface ocean, $k_{surface}$ (1/yr)	9 (Frings et al. 2016) (applies only to radiolarians)	N/A	9 (applies only to radiolarians)	
BSi dissolution rate constant, surface ocean, k_{deep} (1/yr)	24 (Frings et al. 2016) (applies only to radiolarians)	N/A	3 (applies only to radiolarians) (Erez, Takahashi, and Honjo 1982; Berger 1968)	
Apparent BSi solubility, C_{eq} (µM)	350 (Loucaides et al. 2012)	N/A	100 (applies only to radiolarians) (Berger 1968)	350 (applies only to radiolarians)
ε^{30}Si (‰)	diatom: -1.1 (de la Rocha, Brzezinski, and DeNiro 1997; Sutton et al. 2013; Milligan et al. 2004)	sponge: $-4.6 + \frac{27.6}{7.4+[DSi]}$(Hendry et al. 2019)	sponge: $-4.6 + \frac{27.6}{7.4+[DSi]}$(Hendry et al. 2019); radiolarian: -1.1 (Abelmann et al. 2015)	sponge: $-4.6 + \frac{27.6}{7.4+[DSi]}$(Hendry et al. 2019) or extrapolation of Michaelis-Menten relationship for high [DSi]* (Wille et al. 2010; Cassarino et al. 2018); radiolarian: -1.1 (Abelmann et al. 2015)

*Following Wille et al. (2010) and Cassarino et al. (2018), we solve for $\varepsilon^{30}Si = \varepsilon_{tl} + (\varepsilon_p - \varepsilon_E)\left(1 - \frac{\frac{V_{max,P}}{\left(\frac{K_{m,P}}{[DSi]}\right)+1}}{\frac{V_{max,I}}{\left(\frac{K_{m,I}}{[DSi]}\right)+1}}\right)$, where ε_{tl} = -1.34‰ is the fractionation during DSi uptake, (ε_p - ε_E) = -5.39‰ is the difference between fractionation during polymerization (ε_p) and fractionation during efflux (ε_E), $V_{max,P}$ is the maximum polymerization rate (set as the maximum BSi production rate given in the table), $V_{max,I}$ is

the maximum incorporation rate estimated as 9 μmol/hr/mL sponge following Cassarino et al. (2018), $K_{m,P}$ is the half saturation constant of polymerization (set as the K_m value in the table), and $K_{m,I}$ is the half saturation constant of incorporation, calculated as $\frac{V_{max,I}K_{m,P}}{V_{max,P}}$.

Table S2—SIMS δ^{30}Si and δ^{18}O overview statistics

	J1518-48.7	**J1518-92.4**	**J1518-167.9**	**J1518-187.4**
δ^{30}Si analyses				
radiolarian interior				
n analyses	2	4	0	11
median (‰)	0.65	0.25	N/A	-0.98
standard deviation (‰)	0.19	0.59	N/A	0.61
maximum (‰)	0.78	0.80	N/A	0.01
minimum (‰)	0.51	-0.57	N/A	-2.15
radiolarian test wall				
n analyses	2	18	9	16
median (‰)	1.32	0.57	0.70	-0.64
standard deviation (‰)	0.38	0.24	0.47	0.52
maximum (‰)	1.59	1.06	1.15	-0.05
minimum (‰)	1.05	0.13	-0.11	-1.88
spicule				
n analyses	48	13	36	18
median (‰)	0.09	0.24	0.05	-1.03
standard deviation (‰)	0.49	0.26	0.37	0.71
maximum (‰)	1.51	0.70	0.82	0.52
minimum (‰)	-0.98	-0.11	-0.98	-2.40

matrix				
n analyses	33	39	48	51
median (‰)	0.41	0.67	0.52	-0.37
standard deviation (‰)	0.47	0.35	0.47	0.65
maximum (‰)	1.54	1.54	1.60	0.67
minimum (‰)	-0.59	0.09	0.80	-2.10
$\Delta^{30}Si_{sponge\text{-}radiolarian}$ (‰)				
w/ radiolarian test wall median $\delta^{30}Si$	-1.23	-0.33	-0.65	-0.39
w/ radiolarian test wall maximum $\delta^{30}Si$	-1.50	-0.82	-1.1	-0.98
$\delta^{18}O$ analyses				
radiolarian interior				
n analyses		10	2	
median (‰)		26.0	22.6	
standard deviation (‰)		1.1	2.7	
maximum (‰)		27.2	24.5	
minimum (‰)		24.2	20.6	
radiolarian test wall				
n analyses		23	6	
median (‰)		26.1	26.4	
standard deviation (‰)		2.1	1.1	
maximum (‰)		30.4	26.8	
minimum (‰)		22.1	25.8	
spicule				

n analyses		6	6	
median (‰)		28.2	25.1	
standard deviation (‰)		2.8	1.0	
maximum (‰)		31.7	26.0	
minimum (‰)		24.8	23.6	
matrix				
n analyses		24	35	
median (‰)		25.1	24.0	
standard deviation (‰)		2.0	1.0	
maximum (‰)		27..5	26.3	
minimum (‰)		20.6	22.2	

References

Abelmann, Andrea, Rainer Gersonde, Gregor Knorr, Xu Zhang, Bernhard Chapligin, Edith Maier, Oliver Esper, et al. 2015. "The Seasonal Sea-Ice Zone in the Glacial Southern Ocean as a Carbon Sink." *Nature Communications* 6 (September): 8136.

Amo, Yolanda Del, and Mark A. Brzezinski. 1999. "The Chemical Form of Dissolved Si Taken up by Marine Diatoms." *Journal of Phycology* 35 (6): 1162–70.

Berger, W. H. 1968. "Radiolarian Skeletons: Solution at Depths." *Science* 159 (3820): 1237–39.

Cardinal, Damien, Nicolas Savoye, Thomas W. Trull, Frank Dehairs, Elzbieta E. Kopczynska, François Fripiat, Jean-Louis Tison, and Luc André. 2007. "Silicon Isotopes in Spring Southern Ocean Diatoms: Large Zonal Changes despite Homogeneity among Size Fractions." *Marine Chemistry* 106 (1): 46–62.

Cassarino, Lucie, Christopher D. Coath, Joana R. Xavier, and Katharine R. Hendry. 2018. "Silicon Isotopes of Deep Sea Sponges: New Insights into Biomineralisation and Skeletal Structure." *Biogeosciences* 15 (22): 6959–77.

De La Rocha, Christina L. 2003. "Silicon Isotope Fractionation by Marine Sponges and the Reconstruction of the Silicon Isotope Composition of Ancient Deep Water." *Geology* 31 (5): 423–26.

De La Rocha, Christina L., and Michael J. Bickle. 2005. "Sensitivity of Silicon Isotopes to Whole-Ocean Changes in the Silica Cycle." *Marine Geology* 217: 267–82.

De La Rocha, Christina L., Mark A. Brzezinski, and Michael J. DeNiro. 2000. "A First Look at the Distribution of the Stable Isotopes of Silicon in Natural Waters." *Geochimica et Cosmochimica Acta* 64 (14): 2467–77.

Douthitt, C. B. 1982. "The Geochemistry of the Stable Isotopes of Silicon." *Geochimica et Cosmochimica Acta* 46 (8): 1449–58.

Egan, Katherine E., Rosalind E. M. Rickaby, Melanie J. Leng, Katharine R. Hendry, Michaël Hermoso, Hilary J. Sloane, Helen Bostock, and Alex N. Halliday. 2012. “Diatom Silicon Isotopes as a Proxy for Silicic Acid Utilisation: A Southern Ocean Core Top Calibration.” *Geochimica et Cosmochimica Acta* 96 (November): 174–92.

Erez, Jonathan, Kozo Takahashi, and Susumu Honjo. 1982. “In-Situ Dissolution Experiment of Radiolaria in the Central North Pacific Ocean.” *Earth and Planetary Science Letters* 59 (2): 245–54.

Frings, Patrick J., Wim Clymans, Guillaume Fontorbe, Christina L. De La Rocha, and Daniel J. Conley. 2016. “The Continental Si Cycle and Its Impact on the Ocean Si Isotope Budget.” *Chemical Geology* 425 (May): 12–36.

Fripiat, F., A-J Cavagna, F. Dehairs, S. Speich, L. André, and D. Cardinal. 2011. “Silicon Pool Dynamics and Biogenic Silica Export in the Southern Ocean Inferred from Si-Isotopes.” *Ocean Science* 7 (5): 533–47.

Hendry, Katharine R., Lucie Cassarino, Stephanie L. Bates, Timothy Culwick, Molly Frost, Claire Goodwin, and Kerry L. Howell. 2019. “Silicon Isotopic Systematics of Deep-Sea Sponge Grounds in the North Atlantic.” *Quaternary Science Reviews* 210 (April): 1–14.

Hendry, Katharine R., and Laura F. Robinson. 2012. “The Relationship between Silicon Isotope Fractionation in Sponges and Silicic Acid Concentration: Modern and Core-Top Studies of Biogenic Opal.” *Geochimica et Cosmochimica Acta* 81 (March): 1–12.

López-Acosta, María, Aude Leynaert, Jacques Grall, and Manuel Maldonado. 2018. “Silicon Consumption Kinetics by Marine Sponges: An Assessment of Their Role at the Ecosystem Level: Silicate Utilization by Sponges.” *Limnology and Oceanography* 63 (6): 2508–22.

Loucaides, Socratis, Philippe Van Cappellen, Vincent Roubeix, Brivaela Moriceau, and Olivier Ragueneau. 2012. “Controls on the Recycling and Preservation of Biogenic Silica from Biomineralization to Burial.” *Silicon Chemistry* 4 (1): 7–22.

Maldonado, Manuel, Laura Navarro, Ana Grasa, Alicia Gonzalez, and Isabel Vaquerizo. 2011. “Silicon Uptake by Sponges: A Twist to Understanding Nutrient Cycling on Continental Margins.” *Scientific Reports* 1 (July): 30.

Milligan, Allen J., Diana E. Varela, Mark A. Brzezinski, and François M. M. Morel. 2004. “Dynamics of Silicon Metabolism and Silicon Isotopic Discrimination in a Marine Diatomas a Function of pCO2.” *Limnology and Oceanography* 49 (2): 322–29.

Nelson, David M., Paul Tréguer, Mark A. Brzezinski, Aude Leynaert, and Bernard Quéguiner. 1995. “Production and Dissolution of Biogenic Silica in the Ocean: Revised Global Estimates, Comparison with Regional Data and Relationship to Biogenic Sedimentation.” *Global Biogeochemical Cycles*, Soc. Econ. Paleont. Mineral. Spec. Publ., 9 (3): 359–72.

Passow, Uta, Megan A. French, and Maya Robert. 2011. “Biological Controls on Dissolution of Diatom Frustules during Their Descent to the Deep Ocean: Lessons Learned from Controlled Laboratory Experiments.” *Deep Sea Research Part I: Oceanographic Research Papers* 58 (12): 1147–57.

Rahman, S., R. C. Aller, and J. K. Cochran. 2017. “The Missing Silica Sink: Revisiting the Marine Sedimentary Si Cycle Using Cosmogenic 32 Si : The Missing Sedimentary Silica Sink.” *Global Biogeochemical Cycles* 31 (10): 1559–78.

Rocha, Christina L. de la, Mark A. Brzezinski, and Michael J. DeNiro. 1997. “Fractionation of Silicon Isotopes by Marine Diatoms during Biogenic Silica Formation.” *Geochimica et Cosmochimica Acta* 61 (23): 5051–56.

Sarmiento, Jorge L., and Nicolas Gruber. 2006. *Ocean Biogeochemical Dynamics*. Princeton University Press.

Schmidt, Paul, Bellot-Gurlet, Ludovic, Slodczyk, Aneta, Fröhlich, François. 2012. “A hitherto unrecognised band in the Raman spectra of silica rocks: influence of hydroxylated Si–O bonds (silanole) on the Raman moganite band in chalcedony and flint (SiO2).” *Physics and Chemistry of Minerals* 39 (6): 455-464.

Siever, Raymond. 1992. “The Silica Cycle in the Precambrian.” *Geochimica et Cosmochimica Acta* 56 (8): 3265–72.

Strauss, J. V., T. Fraser, M. J. Melchin, T. J. Allen, J. Malinowski, X. Feng, J. F. Taylor, J. Day, B. C. Gill, and E. A. Sperling. 2020. “The Road River Group of Northern Yukon, Canada: Early Paleozoic Deep-Water Sedimentation within the Great American Carbonate Bank.” *Canadian Journal of Earth Sciences*.

Sutton, Jill N., Diana E. Varela, Mark A. Brzezinski, and Charlotte P. Beucher. 2013. “Species-Dependent Silicon Isotope Fractionation by Marine Diatoms.” *Geochimica et Cosmochimica Acta* 104 (March): 300–309.

Tréguer, Paul, and Christina L. De La Rocha. 2013. “The World Ocean Silica Cycle.” *Annual Review of Marine Science* 5: 477–501.

Varela, Diana E., Carol J. Pride, and Mark A. Brzezinski. 2004. “Biological Fractionation of Silicon Isotopes in Southern Ocean Surface Waters.” *Global Biogeochemical Cycles* 18 (1). https://doi.org/10.1029/2003GB002140.

Wille, Martin, Jill Sutton, Michael J. Ellwood, Malcolm Sambridge, William Maher, Stephen Eggins, and Michelle Kelly. 2010. “Silicon Isotopic Fractionation in Marine Sponges: A New Model for Understanding Silicon Isotopic Variations in Sponges.” *Earth and Planetary Science Letters* 292 (3): 281–89.